34th EUROPEAN ROTORCRAFT FORUM

Session: Aircraft Design

PERFORMANCE OF A HOPPING ROTOCHUTE

by

E. Beyer, M. Costello

School of Aerospace Engineering
Georgia Institute of Technology
Atlanta, Georgia 30332

SEPTEMBER 16-19, 2008
LIVERPOOL
ENGLAND

PERFORMANCE OF A HOPPING ROTOCHUTE

Eric Beyer*, Mark Costello$
School of Aerospace Engineering
Georgia Institute of Technology
Atlanta, Georgia 30327

Abstract

The hopping rotochute is a new hybrid micro vehicle that consists of a small coaxial rotor system housed in a lightweight cage. The body is designed to be self righting so that after impacting the ground it passively reorients itself to an upright position. The air vehicle is powered in short bursts so it traverses an area by hopping. Performance is generated using an experimentally validated flight dynamic model capable of predicting the trajectory and orientation while the vehicle is air borne and on the ground. Parametric trade studies varying rotor rotational speed, vehicle mass, and control mass are examined. Through dynamic simulation combined with flight testing it has been shown that the hopping rotochute is a promising new micro vehicle that is well suited to operation in small spaces with complex terrain.

NOMENCLATURE

C_D, C_M : Aerodynamic drag and moment coefficient.
D : Aerodynamic reference distance.
I : Inertia matrix of hopping rotochute about the mass center.
m : Hopping rotochute mass.
L, M, N : Total applied moment components about the mass center in the body reference frame.
p, q, r: Components of angular velocity vector in the body reference frame.
$\mathbf{R}_H$: Skew-symmetric matrix representation of the position vector from the mass center to a point H in the body reference frame.
S : Aerodynamic reference area.
$\mathbf{T}_{BI}$: Transformation matrix from the inertial reference frame to the body reference frame.
$\mathbf{T}_{BR}$: Transformation matrix from the inertial reference frame to the body reference frame.
$\mathbf{T}_{IB}$: Transformation matrix from the body reference frame to the inertial reference frame.
T : Rotor thrust.
u, v, w: Components of mass center velocity vector in the body reference frame.
x, y, z : Components of mass center position vector in an inertial frame.
X, Y, Z : Total applied force components in the body reference frame.
ϕ, θ, ψ : Euler roll, pitch and yaw angles of hopping rotochute.
τ : Rotor lag time constant.

INTRODUCTION

Ground and air robots are playing an increasingly important role in military operations. Potential future applications for micro vehicles include micro surveillance and reconnaissance robots, robots with path finding capability, deception robots, weapon delivery robots, and even robots that search and destroy other enemy robots, to name a few. The key to the success of current and future battlefield robots lies the basic robot configuration being properly tailored to the intended application. An important mission to be tackled by future battlefield robots is exploring small interior and exterior spaces such as caves, the inside of damaged

* Graduate Research Assistant.
$ Sikorsky Associate Professor.

buildings, the exterior perimeter of buildings in cluttered urban settings, etc. Besides being mission capable in these difficult environments, the robots require operations over extended periods of time. These environments are extremely difficult for current micro ground robots and micro air robots. Since these settings are so unpredictable and commonly characterized by very uneven terrain, highly variable walls, openings, and obstacles, micro ground robots find it very difficult to ambulate in a timely and reliable manner. While some specially designed micro ground robots can traverse this type of terrain, they do it very slowly and suffer short range. This has led to substantial investments in micro ground robot ambulation with advanced track systems and legged locomotion. Interior spaces of caves and damaged buildings are small, confined spaces that are problematic for aircraft to fly through without incident. Micro air vehicles operating in this backdrop must be small, highly maneuverable, fly at low speed, and also ideally have hovering capability. While some small rotorcraft and fixed wing micro air vehicles are capable of successful operation in these conditions, they suffer from very short endurance and are unreliable. This has also led to substantial investment in highly maneuverable micro air vehicles that can hover and fly at low speed [1].

New hybrid robots are being created that mix ground ambulation and flight, such as hopping robots [2-6]. Various versions of hopping robots have been proposed such as spring, pneumatically, and propellant driven machines with algorithms for open-loop stable hopping configurations. The hopping robot developed by Spletzer, et al has a self righting capability and is driven by a chemical propulsion design. The main advantage of these mechanical hopping machines is the ability to hop over difficult terrain to navigate and the ability to loiter for long periods of time with minimal energy consumption.

A new hybrid micro vehicle configuration, called the hopping rotochute, is investigated here. The hopping rotochute configuration, shown in Fig. 1, is optimized to operate within small interior spaces. The vehicle is propelled upward by a motor-driven rotor that is powered in short bursts so that the vehicle hops into the air under rotor power and then descends to the ground when unpowered. The mass properties and exterior shape of the main body of the vehicle are designed to be self-righting so independent of the landing orientation, it always rotates into its nominal position once on the ground. To control the direction of movement of the vehicle, an internal mass is rotated around the perimeter of the body to tilt the main body in the desired direction before a given launch. The work reported here investigates the basic performance of this type of vehicle using an experimentally validated simulation model. Flight mechanic characteristics are explored and endurance as a function of energy consumption are documented.

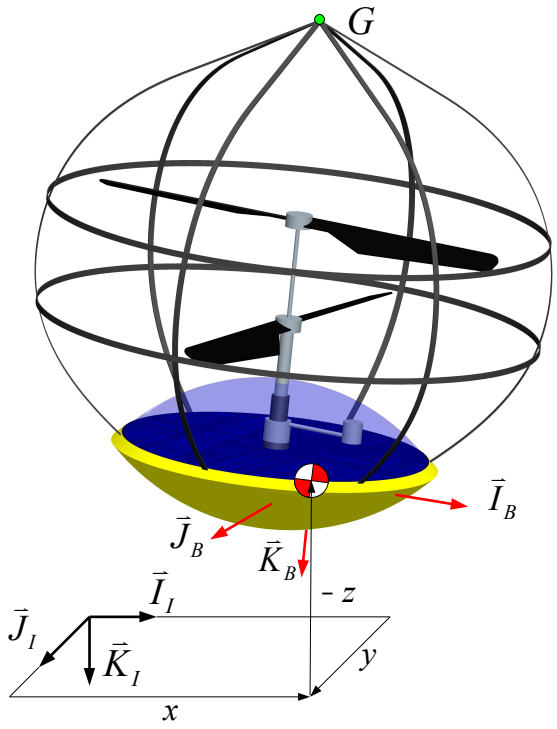

Figure 1 – Hopping Rotochute Model with Associated Reference Frames

VEHICLE DYNAMIC MODEL

The numerical simulation employed in this study is based on a rigid body model of the hopping rotochute with six degrees of freedom. The twelve states describing the motion include the position and velocity of the center of mass as well as the Euler orientation angles and angular rates of the body with respect to the inertial space [7]. The equations of motion describing the dynamics of the hopping rotochute are given in Eqs. (1) through (4).

$$\begin{Bmatrix} \dot{x} \\ \dot{y} \\ \dot{z} \end{Bmatrix} = \left[\mathbf{T}_{IB} \right] \begin{Bmatrix} u \\ v \\ w \end{Bmatrix} \tag{1}$$

$$\begin{Bmatrix} \dot{\phi} \\ \dot{\theta} \\ \dot{\psi} \end{Bmatrix} = \begin{bmatrix} 1 & s_\phi t_\theta & c_\phi t_\theta \\ 0 & c_\phi & -s_\phi \\ 0 & s_\phi / c_\theta & c_\phi / c_\theta \end{bmatrix} \begin{Bmatrix} p \\ q \\ r \end{Bmatrix} \tag{2}$$

$$\begin{Bmatrix} \dot{u} \\ \dot{v} \\ \dot{w} \end{Bmatrix} = \begin{Bmatrix} X/m \\ Y/m \\ Z/m \end{Bmatrix} - \left[\mathbf{S}_B \right] \begin{Bmatrix} u \\ v \\ w \end{Bmatrix} \tag{3}$$

$$\begin{Bmatrix} \dot{p} \\ \dot{q} \\ \dot{r} \end{Bmatrix} = \left[I \right]^{-1} \left[\begin{Bmatrix} L \\ M \\ N \end{Bmatrix} - \left[\mathbf{S}_B \right] \left[I \right] \begin{Bmatrix} p \\ q \\ r \end{Bmatrix} \right] \tag{4}$$

where

$$\mathbf{T}_{IB} = \begin{bmatrix} c_\theta \, c_\psi & s_\phi \, s_\theta \, c_\psi - c_\phi \, s_\psi & c_\phi \, s_\theta \, c_\psi + s_\phi \, s_\psi \\ c_\theta \, s_\psi & s_\phi \, s_\theta \, s_\psi + c_\phi \, c_\psi & c_\phi \, s_\theta \, c_\psi - s_\phi \, c_\psi \\ -s_\theta & s_\phi \, c_\theta & c_\phi \, c_\theta \end{bmatrix}$$

$$\mathbf{S}_B = \begin{bmatrix} 0 & -r & q \\ r & 0 & -p \\ -q & p & 0 \end{bmatrix}$$

The standard shorthand notation is used in the above equations for the trigonometric functions: $\sin(\alpha) \equiv s_\alpha$, $\cos(\alpha) \equiv c_\alpha$, and $\tan(\alpha) \equiv t_\alpha$.

The applied loads expressed in the above equations contain contributions from weight ($_W$), body aerodynamics ($_{BA}$), rotor air loads ($_{RA}$), and contact loads ($_C$). The total forces and moments applied to the vehicle expressed in the body frame are given in Eqs. (5) and (6) respectively.

$$\begin{Bmatrix} X \\ Y \\ Z \end{Bmatrix} = \begin{Bmatrix} X_W \\ Y_W \\ Z_W \end{Bmatrix} + \begin{Bmatrix} X_{BA} \\ Y_{BA} \\ Z_{BA} \end{Bmatrix} + \begin{Bmatrix} X_{RA} \\ Y_{RA} \\ Z_{RA} \end{Bmatrix} + \begin{Bmatrix} X_C \\ Y_C \\ Z_C \end{Bmatrix} \tag{5}$$

$$\begin{Bmatrix} L \\ M \\ N \end{Bmatrix} = \begin{Bmatrix} L_B \\ M_B \\ N_B \end{Bmatrix} + \begin{Bmatrix} L_{BA} \\ M_{BA} \\ N_{BA} \end{Bmatrix} + \begin{Bmatrix} L_{RA} \\ M_{RA} \\ N_{RA} \end{Bmatrix} + \begin{Bmatrix} L_C \\ M_C \\ N_C \end{Bmatrix} \tag{6}$$

The weight is given by

$$\begin{Bmatrix} X_W \\ Y_W \\ Z_W \end{Bmatrix} = mg \begin{Bmatrix} -s_\theta \\ s_\phi \, c_\theta \\ c_\phi \, c_\theta \end{Bmatrix} \tag{7}$$

The aerodynamic force from the body is calculated assuming that drag acts on the body at the center of pressure ($_{CP}$) as shown in Eq. (8).

$$\begin{Bmatrix} X_{BA} \\ Y_{BA} \\ Z_{BA} \end{Bmatrix} = -\frac{1}{2} \rho \, V_{CP} S_B C_{DB} \begin{Bmatrix} u_{CP} \\ v_{CP} \\ w_{CP} \end{Bmatrix} \tag{8}$$

where

$$V_{CP} = \sqrt{u_{CP}^2 + v_{CP}^2 + w_{CP}^2}$$

The aerodynamic moment due to the base about the mass center is calculated as,

$$\begin{Bmatrix} L_{BA} \\ M_{BA} \\ N_{BA} \end{Bmatrix} = [\mathbf{R}_{CP}] \begin{Bmatrix} X_{BA} \\ Y_{BA} \\ Z_{BA} \end{Bmatrix} \quad (9)$$

$$\mathbf{R}_{CP} = \begin{bmatrix} 0 & -WL_{CP} & BL_{CP} \\ WL_{CP} & 0 & -SL_{CP} \\ -BL_{CP} & SL_{CP} & 0 \end{bmatrix}$$

where $\mathbf{R}_{CP}$ is the skew-symmetric matrix representation of the position vector from the mass center to the center of pressure of the body.

The aerodynamic force from the rotor blades is given in Eq. (10).

$$\begin{Bmatrix} X_{RA} \\ Y_{RA} \\ Z_{RA} \end{Bmatrix} = [\mathbf{T}_{BR}] \begin{Bmatrix} 0 \\ 0 \\ -T \end{Bmatrix} \quad (10)$$

$$\mathbf{T}_{BR} = \begin{bmatrix} c_{\theta_R} & s_{\phi_R} s_{\theta_R} & c_{\phi_R} s_{\theta_R} \\ 0 & c_{\phi_R} & -s_{\phi_R} \\ -s_{\theta_R} & s_{\phi_R} c_{\theta_R} & c_{\phi_R} c_{\theta_R} \end{bmatrix}$$

where ϕ_R and θ_R are defined as

$$\phi_R = \phi - \phi_F \quad (11)$$

$$\theta_R = \theta - \theta_F \quad (12)$$

The aerodynamic moment from the rotor blades is given in Eq. (13).

$$\begin{Bmatrix} L_{RA} \\ M_{RA} \\ N_{RA} \end{Bmatrix} = [\mathbf{R}_R] \begin{Bmatrix} X_{RA} \\ Y_{RA} \\ Z_{RA} \end{Bmatrix} +$$

$$[\mathbf{T}_{BR}] \left(-\frac{1}{2} \rho V_R S_R D_R C_{M_R} \right) \begin{Bmatrix} v \\ u \\ 0 \end{Bmatrix} \quad (13)$$

The rotor blades do not instantaneously follow the rotor shaft when the body rotates. To capture this phenomenon, two first order filters are employed to create this lag,

$$\dot{\phi}_F = \frac{\phi - \phi_F}{\tau} \quad (14)$$

$$\dot{\theta}_F = \frac{\theta - \theta_F}{\tau} \quad (15)$$

The contact forces and moments that act on the base during ground impact are calculated based on a soft contact model originally developed by Goyal, Pinson, and Sinden [8,9]. The model uses vertices located around the perimeter of the body (see Fig. 2) to calculate the contact forces between the hopping rotochute and the ground (assumed to be flat for this study). The contact forces associated with each contact point has two components: a normal component $\left(\vec{F}_n\right)$ along the ground normal and a frictional component $\left(\vec{F}_t\right)$ in the tangential plane of contact. Each vertice has a normal and tangential spring attached to it along with a normal and tangential damper as shown in Fig. 3.

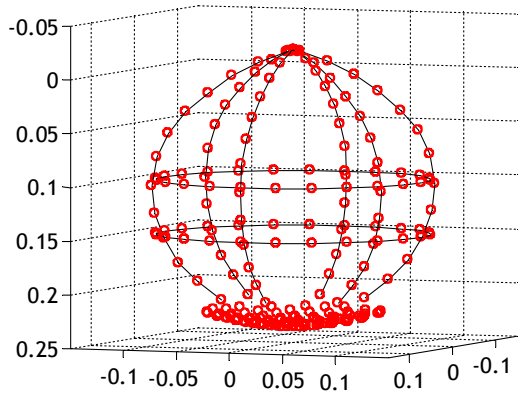

Figure 2 – Example Vertice Arrangement for Soft Contact Model

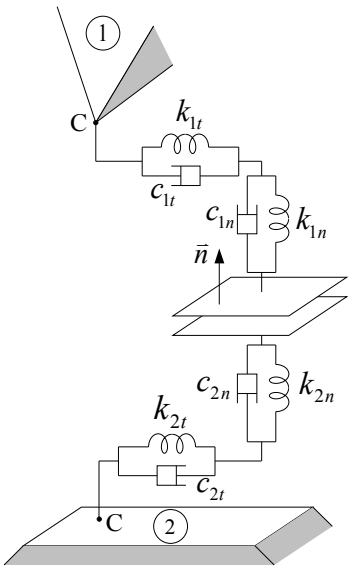

Figure 3 – Spring and Damper Schematic for Soft Contact Model

The spring constant along the normal and tangential directions are defined as k_{1n} and k_{1t} respectively while the damper constants are defined as c_{1n} and c_{1t}. The ground also has similar springs and dampers in these two directions with constants k_{2n}, k_{2t}, c_{2n}, and c_{2t}. Assuming all dampers are non-zero, the force in the normal and tangential directions associated with a given vertice v is,

$$\vec{F}_{n_v} = -\vec{b}_{n_v} \tag{16}$$

$$\vec{F}_{t_v} = -\vec{b}_{t_v} + c^* \Delta \vec{w}_{t_v} \tag{17}$$

where

$$c^* = \frac{c_{1t} c_{2t}}{c_{1t} + c_{2t}}$$

$$\vec{b}_{n_v} = \frac{1}{c_{1n} + c_{2n}} \left(c_{2n} k_{1n} \vec{s}_{1n_v} - c_{1n} k_{2n} \vec{s}_{2n_v} + c_{1n} c_{2n} \Delta \vec{u}_{n_v} \right)$$

$$\vec{b}_{t_v} = \frac{1}{c_{1t} + c_{2t}} \left(c_{2t} k_{1t} \vec{s}_{1t_v} - c_{1t} k_{2t} \vec{s}_{2t_v} + c_{1t} c_{2t} \Delta \vec{u}_{t_v} \right)$$

The difference in the absolute velocity of vertice v and the ground along the normal and tangential directions are given as $\Delta \vec{u}_{1n_v}$ and $\Delta \vec{u}_{1t_v}$ respectively. The states $\vec{s}_{1n_v}$ and $\vec{s}_{2n_v}$ track the lengths of the normal springs, while $\vec{s}_{1t_v}$ and $\vec{s}_{2t_v}$ track the lengths of the tangential springs of each contact point. The tangential force of vertice v is based on the relationship given in Eq. (18).

$$\frac{\left|\vec{b}_{t_v}\right|}{\left(1 + \lambda_v c^*\right)} \le \mu \left|\vec{b}_{n_v}\right| \tag{18}$$

If the relation $\left|\vec{b}_{t_v}\right| \le \mu \left|\vec{b}_{n_v}\right|$ holds true, then a state of stick exists and the variables are calculated as,

$$\lambda_v = 0 \tag{19}$$

$$\Delta \vec{w}_{t_v} = 0 \tag{20}$$

$$\vec{F}_{t_v} = -\vec{b}_{t_v} \tag{21}$$

If, on the other hand $\left|\vec{b}_{t_v}\right| > \mu \left|\vec{b}_{n_v}\right|$, the variables are calculated using the following equations,

$$\lambda_v = \frac{\left|\vec{b}_{t_v}\right| - \mu \left|\vec{b}_{n_v}\right|}{c^* \mu \left|\vec{b}_{n_v}\right|} \tag{22}$$

$$\Delta \vec{w}_{t_v} = \frac{\lambda_v \vec{b}_{t_v}}{\left(1 + \lambda_v c^*\right)} \tag{23}$$

$$\vec{F}_{t_v} = \frac{-\vec{b}_{t_v}}{\left(1 + \lambda_v c^*\right)} \tag{24}$$

Hence, the contact force and moment applied to the base body in the body frame about the mass center are given as

$$\begin{Bmatrix} X_C \\ Y_C \\ Z_C \end{Bmatrix} = [\mathbf{T}_{BI}] \sum_{v=1}^{NV} \left(\vec{F}_{n_v} + \vec{F}_{t_v} \right) \quad (25)$$

$$\begin{Bmatrix} L_C \\ M_C \\ N_C \end{Bmatrix} = \sum_{v=1}^{NV} \left(\left[\mathbf{R}_{V_v} \right] [\mathbf{T}_{BI}] \left(\vec{F}_{n_v} + \vec{F}_{t_v} \right) \right) \quad (26)$$

where NV is the number of vertices. The state of the springs associated with each vertice in the contact model is tracked with the following differential equations,

$$\dot{\vec{s}}_{1n_v} = \frac{c_{2n}}{\mathrm{c}_n} \Delta \vec{u}_{n_v} - \frac{1}{\mathrm{c}_n} \left(k_{1n} \vec{s}_{1n_v} + k_{2n} \vec{s}_{2n_v} \right) \quad (27)$$

$$\dot{\vec{s}}_{1t_v} = \frac{c_{2t}}{\mathrm{c}_t} \left(\Delta \vec{u}_{t_v} - \Delta \vec{w}_{t_v} \right) - \frac{1}{\mathrm{c}_t} \left(k_{1t} \vec{s}_{1t_v} + k_{2t} \vec{s}_{2t_v} \right) \quad (28)$$

$$\dot{\vec{s}}_{2n_v} = \frac{-c_{1n}}{\mathrm{c}_n} \Delta \vec{u}_{n_v} - \frac{1}{\mathrm{c}_n} \left(k_{1n} \vec{s}_{1n_v} + k_{2n} \vec{s}_{2n_v} \right) \quad (29)$$

$$\dot{\vec{s}}_{2t_v} = \frac{-c_{1t}}{\mathrm{c}_t} \left(\Delta \vec{u}_{t_v} - \Delta \vec{w}_{t_v} \right) - \frac{1}{\mathrm{c}_t} \left(k_{1t} \vec{s}_{1t_v} + k_{2t} \vec{s}_{2t_v} \right) \quad (30)$$

where

$$\mathrm{c}_n = c_{1n} + c_{2n}$$

$$\mathrm{c}_t = c_{1t} + c_{2t}$$

VEHICLE DESCRIPTION

The hopping rotochute used in this study is shown in Fig. 4 and consists of an EPS foam core, a polyurethane foam cushion, a carbon fiber cage, an aluminum motor mount, an internal mass, and a gearbox and rotor blades which were taken from an Air Hogs Reflex Micro Helicopter. Both sets of rotor blades are powered by a single small brushed dc motor while the internal mass is controlled by a micro servo. The carbon fiber cage has an average diameter of 25.4 cm and was designed so the vehicle always uprights itself while on the ground.

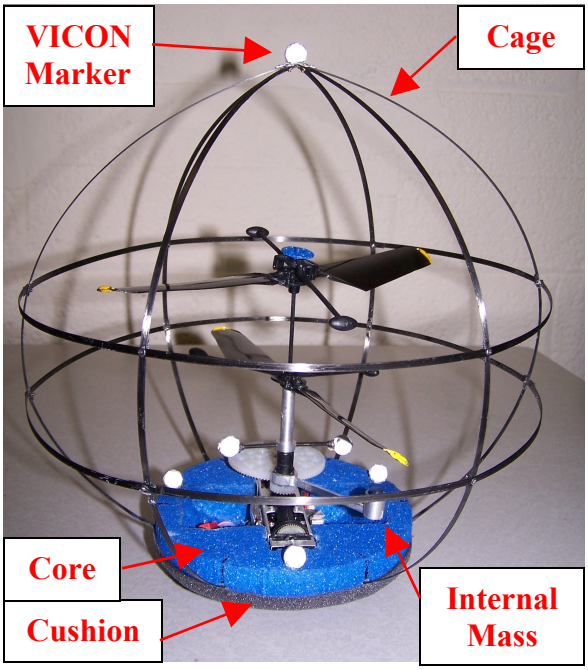

Figure 4 – Hopping Rotochute with VICON Markers

MODEL VALIDATION

The aerodynamic characteristics of the hopping rotochute rotors were obtained via a rotor test stand as shown in Fig. 5. The rotor test stand consists of an aluminum bar that can pivot about an adjustable-height pipe. The hopping rotochute was attached to one end of the aluminum bar while a rod was attached to the other. As the rotors are powered, the rod pushes against a scale, which measures the thrust being produced at a given rotor speed. The rotor speed was measured using a tachometer while multimeters were employed to measure the current and voltage. The thrust, current, and voltage were measured at several rotor heights above the ground (10.2 - 38.1 cm) and rotor speeds (up to 2100 rpm). The results are presented in Figs. 6 through 8. The power was also calculated as a function of height and rotor speed and plotted in Fig. 9. As shown, the thrust, current, and

potential increase in a quadratic fashion with rotor speed. It is also interesting to note the in-ground-effect and out-of ground-effect of this system. At a height of 30.5 cm, about 1.5 times the rotor radius, the system reaches out-of ground-effect.

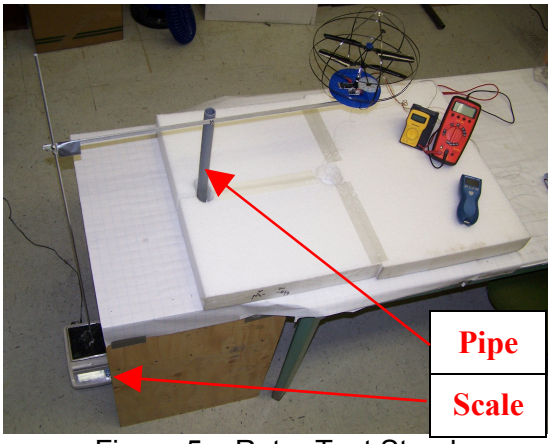

Figure 5 – Rotor Test Stand

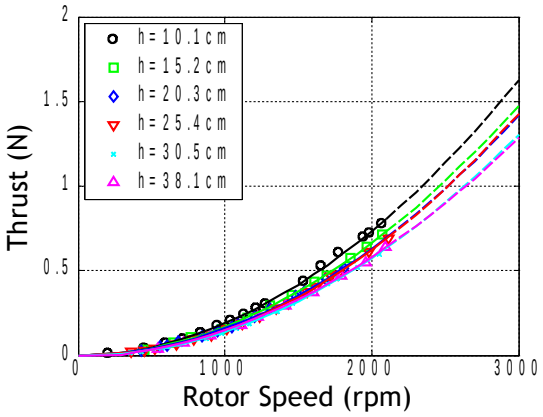

Figure 6 – Thrust versus RPM

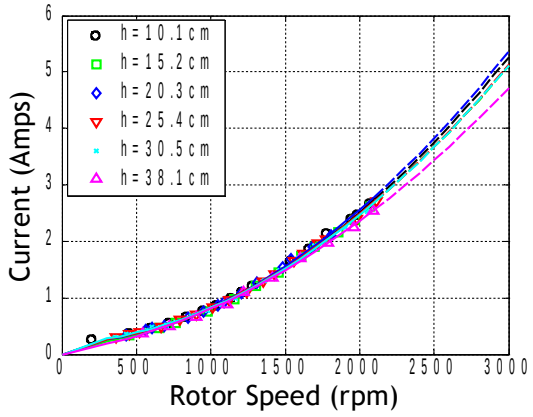

Figure 7 – Current versus RPM

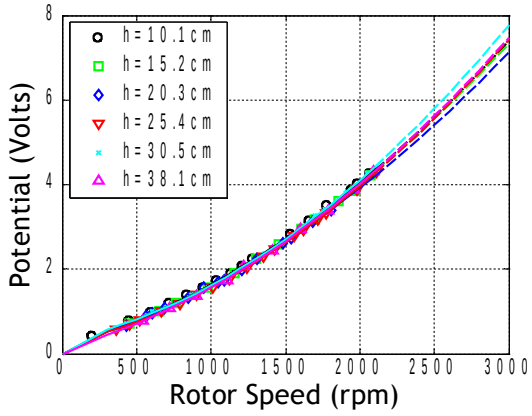

Figure 8 – Potential versus RPM

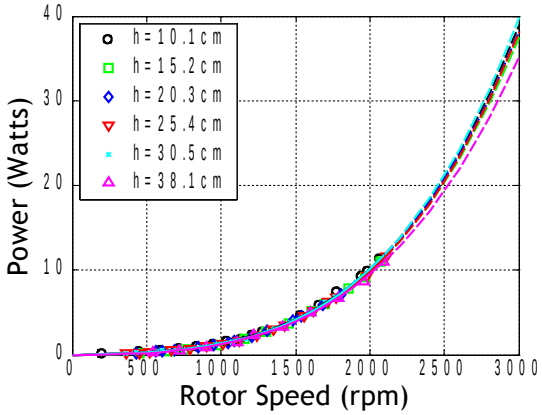

Figure 9 – Power versus RPM

The rotor lag time constant was experimentally obtained by video-taping the hopping rotochute while it was pitched quickly by 90 deg about a point on the base. The pitch angle of the body and the angle of the tip path plane were measured throughout the video footage and this data was compared to a first order filter to determine the time constant. The rotor lag time constant was found to be 0.2.

The contact model requires the values of the spring constant (k) and the damping coefficient (c) of both the foam cushion material on the bottom of the hopping rotochute and the carpet covering the ground. In addition, the coefficient of friction, μ, is needed between these two materials. Three different procedures were

used for the determination of these values. In order to find the spring constant, material samples were placed on a scale and deflected a known amount to find the force exerted. Using the relationship $F = -kx$, the spring constants were determined to be 212 N/m for the polyurethane foam and 120 N/m for the carpet. The coefficient of friction was obtained by placing a weight on a foam sample and moving it at a constant speed across carpet while measuring the force. The coefficient of friction between the polyurethane foam and the carpet was found to be 3.0.

To obtain the damping coefficients, a drop test stand was created as shown in Fig. 10. The drop test stand consists of two pieces: a stand and a slider. The stand was made of a plywood structure with a small stainless steel tube attached at the top and a material sample at the bottom. The slider consists of a long, smaller diameter stainless steel tube which was connected to a curved base with a material sample attached to it. For each material, the slider was lifted to a height of 0.3 m and released. The motion was recorded using a VICON motion capture system. The motion captured from the VICON system was compared with simulation results using the same initial conditions and mass properties as well as the spring constant and friction coefficient obtained from the test described earlier. The damping coefficients were adjusted until the VICON data and simulation results correlated. An example result is presented in Fig. 11, where the red points represent the data from the VICON system and the black line is the simulated result. The damping coefficient of both the polyurethane foam and the carpet were determined to be 0.7 N-s/m.

In order to validate the flight dynamics part of the model, VICON markers were placed on the hopping rotochute at 6 different locations as shown in Fig. 4.

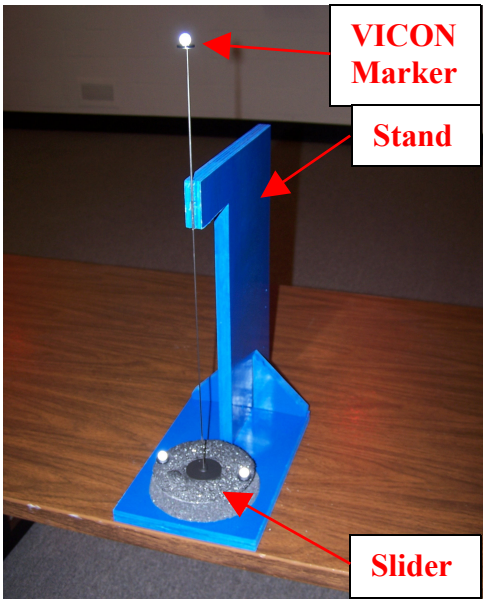

Figure 10 – Drop Test Stand

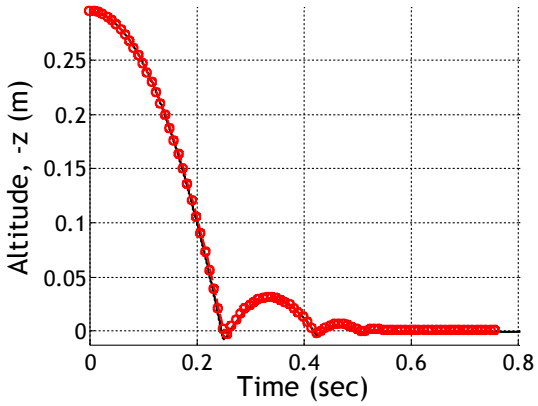

Figure 11 – Altitude versus Time (Dropping Foam onto Carpet

Two of the markers were attached to the lower shaft which allowed for the determination of the rotor speed, while the remaining markers were used to calculate the states of the vehicle. The data collected from the VICON motion capture system was compared to that of the simulation results and the body drag and rotor moment coefficients were varied until correlation occurred. The body aerodynamic drag coefficient and the rotor aerodynamic moment coefficient were determined to be 1.0 and 1.0 respectively. The time histories of an example trajectory (hop) using the VICON system as well as that from the

simulation are shown in Fig. 12 through 22. In these charts, the red line represents the VICON data and the black line represents the simulation results.

As shown in Fig. 12-15, the mass center position versus time from the VICON data and the simulation match up well. For this particular hop, the hopping rotochute reached an altitude of 0.75 m at 1.7 s with a total range of 1.8 m. The pitch angle versus time is given in Fig. 16. Although the pitch angle recorded from this particular hop is slightly different than that of the simulation, it is believed the general trend is captured since this angle was validated with other captured data. As shown in Figs. 17 through 19, the velocity and angular velocity time histories correlate well. Figure 20 presents the rotor speed profiles associated with the VICON and simulation results. The rotor speed calculated from the VICON data is conservative (due to marker exclusions) and has a time lag due to the calculation routine. Hence, although the rotor speed profile from the simulation looks more aggressive than that calculated from the VICON system, the two actually match up quite well when these two considerations are taken. Figures 21 and 22 show the thrust and power time histories from the simulation results which fluctuate between 0.25 and 0.75 s due to the change in rotor height.

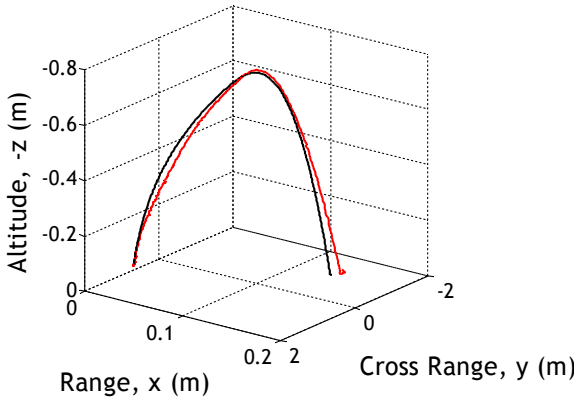

Figure 12 – Range versus Cross Range versus Altitude

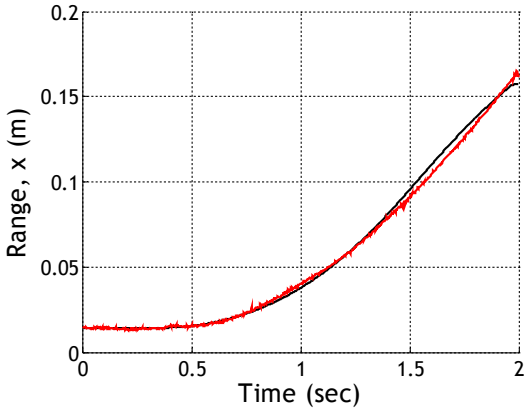

Figure 13 – Range versus Time

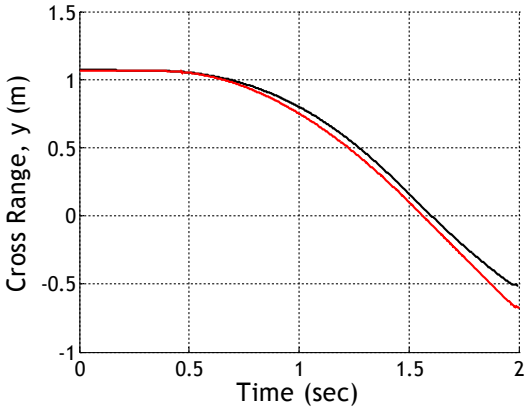

Figure 14 – Cross Range versus Time

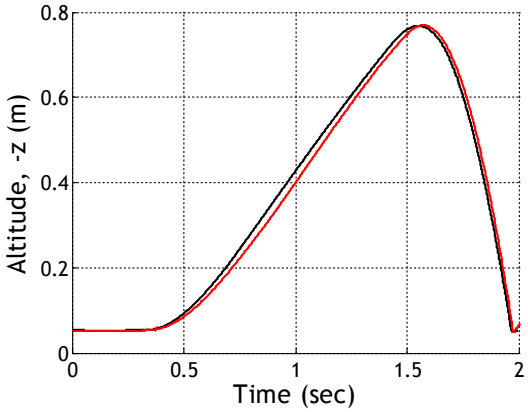

Figure 15 – Altitude versus Time

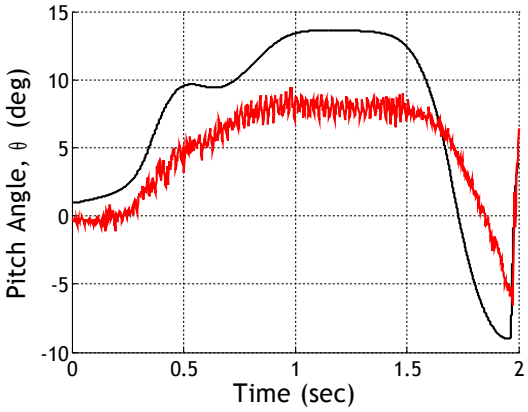

Figure 16 – Pitch Angle versus Time

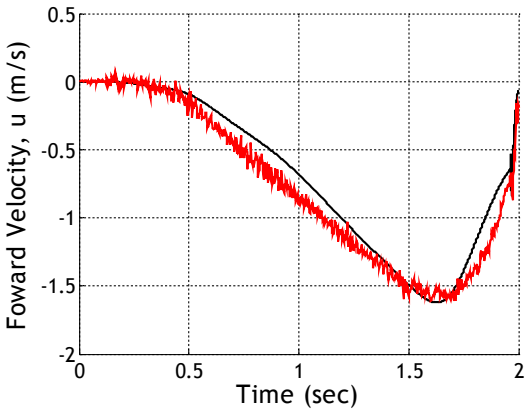

Figure 17 – Forward Velocity versus Time

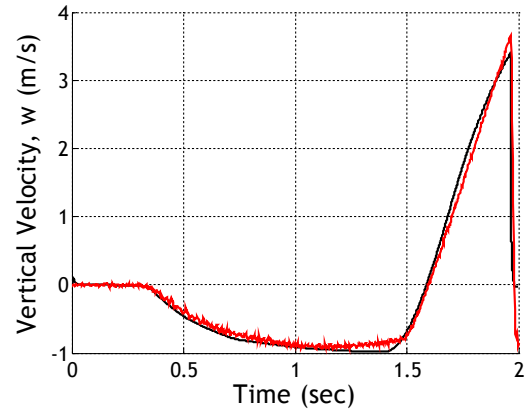

Figure 18 – Vertical Velocity versus Time

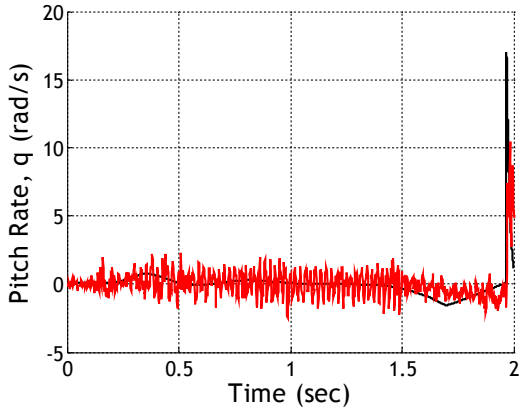

Figure 19 – Pitch Rate versus Time

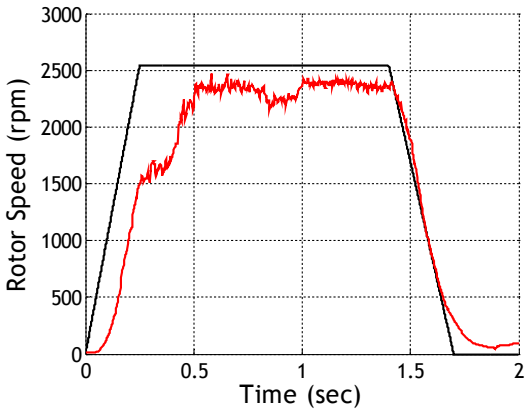

Figure 20 – Rotor Speed versus Time

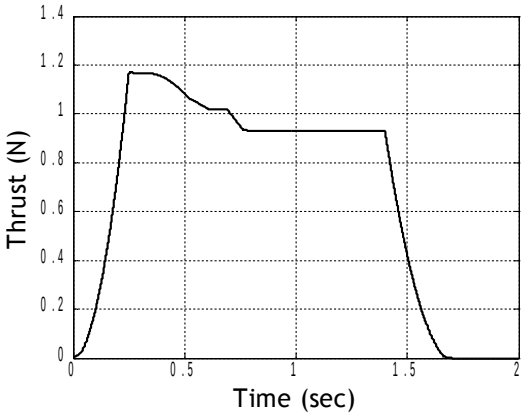

Figure 21 – Thrust versus Time

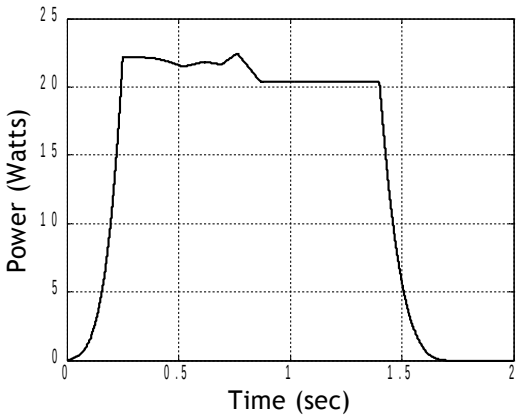

Figure 22 – Power versus Time

MODEL PERFORMANCE

The flight characteristics of the hopping rotochute are highly dependent on the mass properties, battery size, rotor speed, as well as the internal mass location and weight. The mass properties of the hopping rotochute excluding the internal mass and battery are outlined in Table 1.

Table 1 – Hopping Rotochute Mass Properties

Property	Value	Units
m	64.6	g
$x_{G\rightarrow CG}$	0	cm
$y_{G\rightarrow CG}$	0	cm
$z_{G\rightarrow CG}$	17.4	cm
I_{XX}	30.7	g-cm^2
I_{YY}	32.5	g-cm^2
I_{ZZ}	7.4	g-cm^2
I_{XY}	0	g-cm^2
I_{XZ}	0	g-cm^2
I_{YZ}	0	g-cm^2

The properties of the batteries used in this study are given in Table 2.

The total range was also calculated for each trade study which involves multiplying the range achieved by one hop by the number of hops that could be attained given a certain battery size. The number of hops is calculated by dividing the battery size (mAh) by the value obtained by integrating the current versus time curve for a single hop.

Table 2 – Battery Properties

Battery Size (mAh)	Mass (g)
250	13.7
300	19.8
480	24.6

For all trade studies, the rotor speed was activated for 1s at the desired speed as shown in Fig. 23. The slope of the upward and downward part is 10,000 rpm/s and -10,000 rpm/s respectively as is characteristic for this system (see Fig. 20)

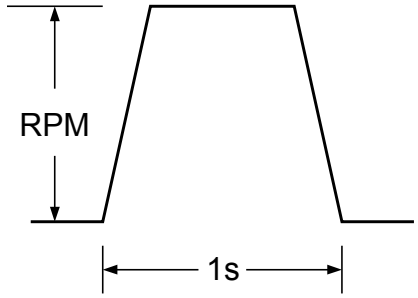

Figure 23 – Rotor Speed Profile

For the first trade study, time simulations were ran with different sized batteries while varying the internal mass (IM) weight and location as well as the rotor speed. The rotor speed was varied from 2000 rpm to 4000 rpm in 100 rpm increments while internal mass weights of 2 g, 4 g, 6 g, 8 g, and 10 g were used at locations of 0 cm, 1.27 cm, 2.54 cm, 3.81 cm, 5.08 cm, and 6.35 cm. For the 250 mAh battery, the total mass of the system was 80.3, 82.3, 84.3, 86.3, 88.3 g while using the 2 g, 4 g, 6 g, 8 g, and 10 g internal mass respectively. The system mass center location along $\vec{I}_B$, $x_{G\rightarrow CG}$, varied from 0.16 cm to 0.72 cm depending on the internal mass used. The resulting curves from this trade study associated with the 250 mAh battery are given in Fig. 24 through 26.

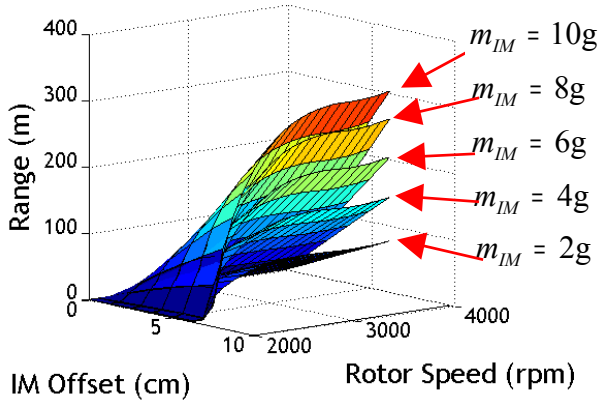

Figure 24 – IM Offset versus Rotor Speed versus Range using 250 mAh Battery

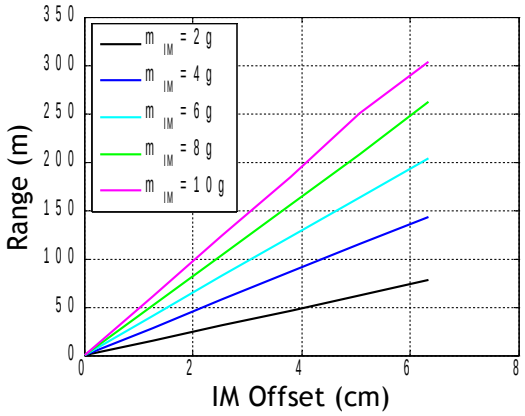

Figure 25 – IM Offset versus Maximum Range using 250 mAh Battery

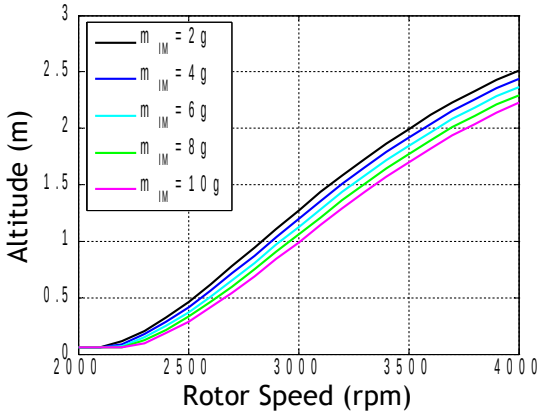

Figure 26 – Rotor Speed versus Altitude for using 250 mAh Battery

As shown in Fig. 24, the total range increases as the internal mass weight is increased, which is an exactly opposite trend when considering conventional air vehicles. The increased internal mass weight allows the body to settle at a higher initial launch angle and creates a larger moment arm between the mass center of the system and the point where the thrust vector acts. Combined, these two parameters allow the heavier hopping rotochute to actually achieve more range. Figure 24 also demonstrates that at low rotor speeds the range increases significantly as the rotor speed is increased and then plateaus at a certain rotor speed depending on the weight of the internal mass used. The range increases linearly with the internal mass offset as shown in Fig. 24 and 25. Figure 25 shows the total range achieved versus internal mass offset at the rotor speed which gives the maximum range (4000 rpm for each case). For this particular trade study, the maximum total range of 304 m occurs while using the 10 g internal mass at an offset of 6.35 cm with a rotor speed of 4000 rpm.

The maximum altitude achieved by the hopping rotochute is dependent on the internal mass weight and the rotor speed. Figure 26 shows this trend when using the 250 mAh battery. The lower weight systems achieve higher altitudes as does larger rotor speeds.

Similar trends occur when the hopping rotochute is powered with larger sized batteries. Figures 27 through 29 are associated with the 300 mAh battery whereas Figs. 30 through 32 are results from the 480 mAh battery.

Although one would expect that a 20% increase in the battery size (from 250 mAh to 300 mAh) would result in about a 20% increase in the range, this is not the case. As shown in Fig. 28, the maximum range for the 300 mAh battery is 316 m which occurs when using the 10 g internal mass with a 6.35 cm offset at 4000 rpm. This is only a

4% increase over the maximum range achieved by the 250 mAh battery. The problem is that the weight of the battery increased by 45%, which makes the mass of the hopping rotochute heavier. In addition the larger system mass makes the initial launch angle and moment arm from the mass center to the thrust vector location smaller. This trend is also evident when considering the 480 mAh battery where the battery size increased by 92% compared to the 250 mAh battery, but the maximum total range only increased by 50% to 456 m.

As shown in Figs. 26, 29, and 32, the maximum height achieved by the hopping rotochute decreases when using larger battery sizes due to the increased system weight.

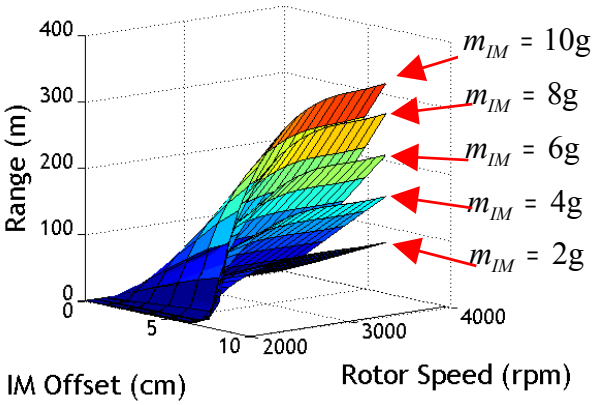

Figure 27 – IM Offset versus Rotor Speed versus Range using 300 mAh Battery

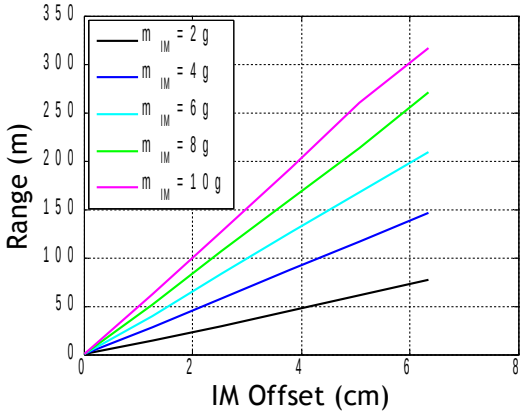

Figure 28 – IM Offset versus Maximum Range using 300 mAh Battery

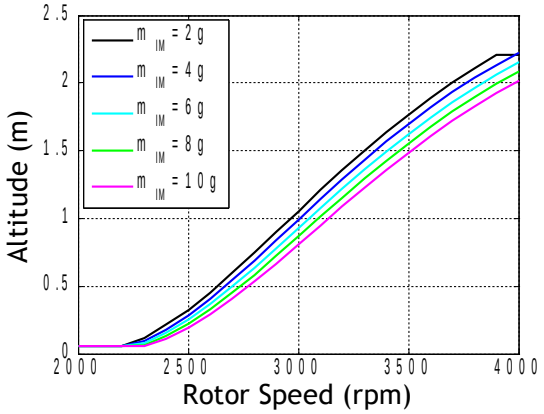

Figure 29 – Rotor Speed versus Altitude for using 300 mAh Battery

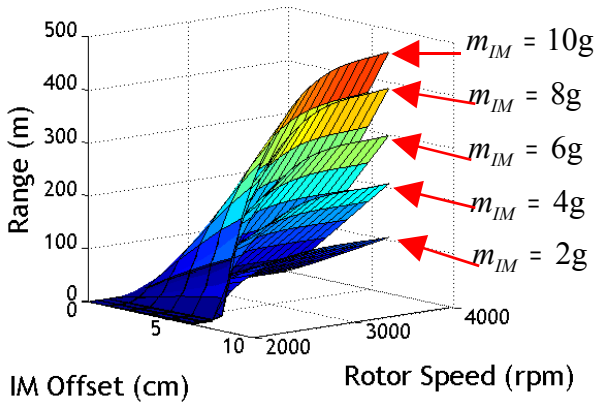

Figure 30 – IM Offset versus Rotor Speed versus Range using 480 mAh Battery

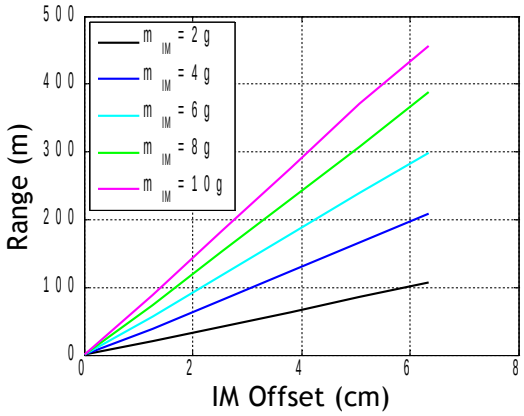

Figure 31 – IM Offset versus Maximum Range using 480 mAh Battery

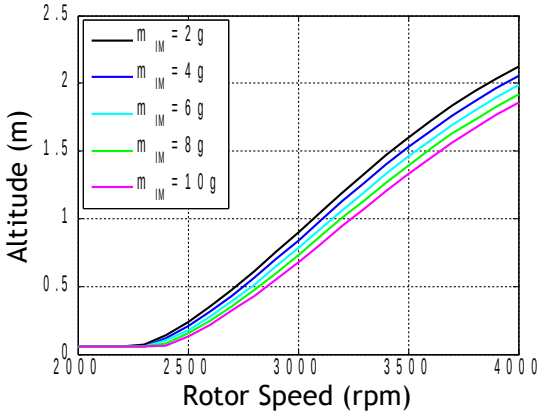

Figure 32 – Rotor Speed versus Altitude for using 480 mAh Battery

The number of hops increases with larger battery sizes as shown in Fig. 33. The number of hops also decreases as a function of rotor speed due to the higher energy usage at increased rotor speeds. Hence at the maximum total range, the hopping rotochute hops 220, 263, 420 times when considering the 250, 300, and 480 mAh battery respectively.

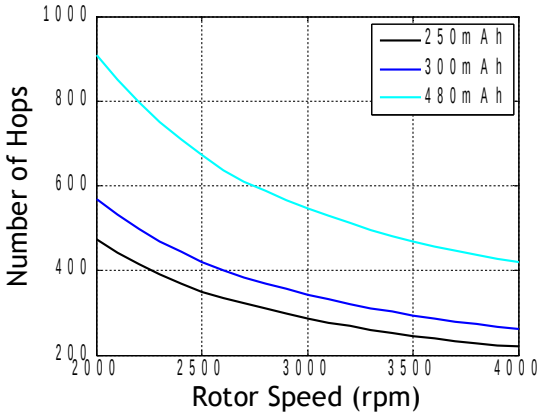

Figure 33 – Rotor Speed versus Number of Hops using 250, 300, 480mAh Battery.

As mentioned earlier and shown in the charts above, the total mass of the hopping rotochute influences the flight characteristics of the vehicle. To get a better understanding of this behavior, the hopping rotochute mass and internal mass weight was reduced proportionally for a given internal mass offset so the mass center remained the same as the total weight increased. The total system weights used in this trade study are 70, 80, 90, and 100 percent of those from the 250 mAh battery system with an internal mass weight of 6 g. This amounts to system masses of 59, 67.4, 75.8, and 84.2 g respectively. The internal mass offset was again set to 0, 1.27, 2.54, 3.81, 5.08, and 6.35 cm which amounts to system mass center locations along $\vec{I}_B$ of 0, 0.09, 0.18, 0.27, 0.36, and 0.45 cm. The results of this trade study are presented in Figs. 34 and 35.

The optimum rotor speed for the maximum range associated with the 59, 67.4, 75.8, and 84.2 g systems were found to be 2500, 2800, 3700, and 4000 rpm respectively. The total range at these rotors speeds are shown in Fig. 34 with the maximum being 259, 234, 220, and 203 m for the different hopping rotochute systems. Hence for the same mass center location, a lighter hopping rotochute provides a greater range.

As expected, the lower weight systems are also able attain more altitude as shown in Fig. 35. The maximum altitude occurs at 3.3, 3, 2.7, and 2.4 m for the 59, 67.4, 75.8, and 84.2 systems respectively.

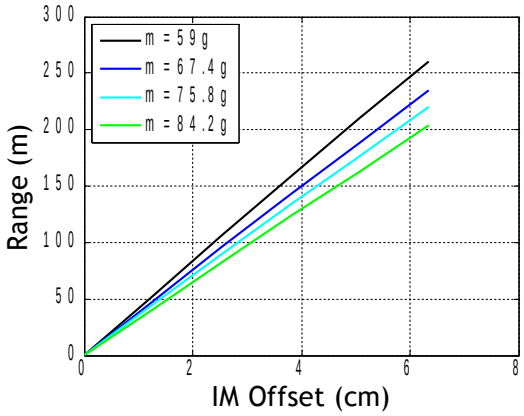

Figure 34 – IM Offset versus Maximum Range using 250 mAh Battery

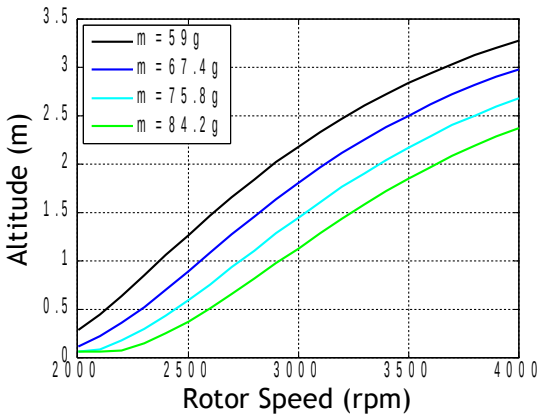

Figure 35 – Rotor Speed versus Altitude using 250 mAh Battery

As discussed above, the internal mass offset has a drastic effect on the total range that can be achieved. To demonstrate this effect, a trade study was performed on a hopping rotochute system with a 250 mAh battery and an internal mass of 6 g at an offset of 0, 1.27, 2.54, 3.81, 5.08, 6.35, 12.7, 25.4, 38.1, 50.8, 63.5 cm. The results are presented in Fig. 36 for the rotor speeds of 3400, 3500, 3600, 3700, and 3800 rpm. As shown, the total range greatly increases as the internal mass offset is increased and then plateaus out at approximately 40 cm. The maximum range is obtained at 50.8 cm with a value of 724, 744, 757, 769, and 778 m associated with rotor speeds of 3400, 3500, 3600, 3700, and 3800 respectively.

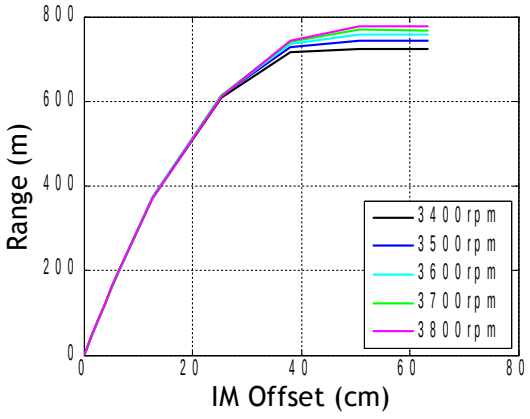

Figure 36 – IM Offset versus Range using 250 mAh Battery

The internal mass offset also greatly effects the maximum attained altitude as shown in Fig. 37.

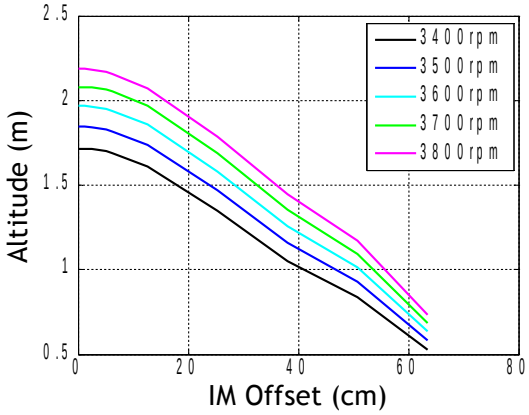

Figure 37 – IM Offset versus Altitude using 250 mAh Battery

CONCLUSIONS

Through an integrated sequence of flight testing and dynamic simulation, the hopping rotochute has been shown to be a promising new hybrid ground/air vehicle that is specifically designed to robustly traverse difficult environments such as caves and damaged buildings. The exterior shape as well as the low mass center allow the hopping rotochute to always upright itself once on the ground, a feature that most current micro air vehicles are lacking. The internal mass, which is able to rotate around the perimeter of the base, allows the vehicle to hop in any given direction over large obstacles which hamper typical ground vehicles. Since vehicle hopping is caused by a coaxial rotor system, the RPM profile for a hop significantly drives the resulting trajectory and power drain. Other key parameters governing hopping performance are vehicle weight, control weight, and internal moving mass offset distance. For the constructed prototype, the vehicle is capable of 250 hops which achieves a range of 300 m on a single 250 mAh battery.

REFERENCES

[1] M. Costello, "Challenges Facing Micro Air Vehicle Flight Dynamics and Controls Engineers," *AIAA Aerospace Sciences Meeting and Exhibit*, Reno, NV, Paper Number 2008-0513, 2008.

[2] J. Cham, M. Cutkosky, “Dynamic Stability of Open-Loop Hopping,” *Journal of Dynamic Systems, Measurement, and Control*, Vol. 129, pp 275-284, May 2007.

[3] B. Seth, P. Seshu, P. Shanmuganathan, V. Vichare, P. Raj “Search for Initial Conditions for Sustained Hopping of Springy-Leg Offset Mass Hopping Robot,” *Journal of Dynamic Systems, Measurements, and Control*, Vol 129, July 2008.

[4] Y. Zhu, E. Barth, “An Energetic Control Methodology for Exploiting the Passive Dynamics of Pnuematically Actuated Hopping,” *Journal of Dynamic Systems, Measurement, and Control*, Vol 130, July 2008.

[5] B. Spletzer, G. Fischer, L. Marron, M. Martinez, M. Kuehl, J. Feddema, “Hopping Robot,” U.S. Patent 6247546, June 2001.

[6] N. Delson, “Dynamic Legged Robot,” U.S. Patent 7168513, January 2007.

[7] B. Etkin, *Dynamics of Atmospheric Flight*, Wiley, New York, 1972.

[8] S. Goyal, E. Pinson, F. Sinden, “Simulation of Dynamics of Interacting Rigid Bodies Including Friction I: General Problem and Contact Model,” *Engineering with Computers*, Vol. 10, pp. 162-174, 1994.

[9] S. Goyal, E. Pinson, F. Sinden, “Simulation of Dynamics of Interacting Rigid Bodies Including Friction II: Software System Design and Implementation,” *Engineering with Computers*, Vol. 10, pp. 175-195, 1994.